Thermodynamic, Structural, and Piezoelectric Properties of Adatom-Doped Phosphorene and Its Applications in Smart Surfaces

Lou Li,[1] Huiying Cao,[1] Bo Xu,[1] Junkai Deng,[1,*] Jingran Liu,[2] Yilun Liu,[2] Xiangdong Ding,[1] Jun Sun,[1] and Jefferson Zhe Liu[3,†]

[1] *State Key Laboratory for Mechanical Behavior of Materials, Xi'an Jiaotong University, Xi'an 710049, China*

[2] *State Key Laboratory for Strength and Vibration of Mechanical Structures, School of Aerospace Engineering, Xi'an Jiaotong University, Xi'an 710049, China*

[3] *Department of Mechanical Engineering, The University of Melbourne, Parkville, VIC 3010, Australia*

(Received 15 August 2019; revised manuscript received 16 March 2020; accepted 28 April 2020; published 26 May 2020)

Engineering the surface morphology is an effective way to obtain specific functionalities in applications of smart surfaces. Developing two-dimensional (2D) smart materials, which can undergo morphology changes under appropriate external stimuli, is a promising route to pursue for smart-surface design. In the work presented here, using density-functional-theory calculations, we systematically study the thermodynamic stability, crystal structure, and piezoelectric properties of black phosphorene (black P) doped with metallic atoms on one side with different concentrations. Particularly, Li-doped black P (P_4Li_2) has a d_{31} value of 6.28 pm/V, which is at least 4 times larger than that of any other 2D piezoelectric material. Via finite-element-method simulations, we show a P_4Li_2-based prototype design for obtaining a surface-morphology change under a vertical electric field. The surface swelling pattern can be detected by human fingers with an appropriate design of the geometry. This demonstrates the promise of 2D piezoelectric materials for use in smart-surface applications.

DOI: 10.1103/PhysRevApplied.13.054061

I. INTRODUCTION

Smart surfaces, which are designed to exhibit certain functionalities and performance under appropriate external stimuli, have attracted significant interest in recent years [1–7]. Engineering the surface topography is a popular and effective approach to providing some desirable functionalities [8], such as wettability [9], adhesion [10], control of aerodynamic drag [11], and molecular adsorption [12]. The design of surface topographies that are responsive to external stimuli holds great potential for applications such as tactile displays [13], controllable optical reflection [14], and reversible control of interface properties [9,10,12]. There is a growing demand for research into finding appropriate materials for use in the design of such smart surfaces.

Two-dimensional (2D) actuation and active materials are liable to exhibit shape or morphology changes under external stimuli [15–18]. Using 2D actuation and active materials in smart-surface design is a natural and promising solution. There are several advantages. First, 2D materials are atomically thin. Advances in assembly technology in the past few years allow us to integrate different 2D materials in a layer-by-layer manner, producing large-area thin-film structures [19–21], which could be suitable for smart-surface applications. Second, 2D materials are often mechanically flexible and robust [22–25]. Third, through surface functionalization, the properties of 2D materials can be designed and significantly improved [15,26]. Among 2D actuation and active materials, 2D piezoelectric materials have received the most research attention [27–30].

If we were to adopt the popular layer-by-layer heterostructures to integrate 2D piezoelectric materials with electrodes (such as graphene), the piezoelectric coefficients d_{33}, d_{31}, and d_{32} would determine the actuation and active performance under a vertical electric field. However, the intrinsic displacement in the normal direction is unlikely to be large enough, due to the nanosized thickness and the finite value of d_{33}. Another strategy is to utilize the elastic buckling displacement in the vertical direction that occurs when the in-plane strain is above some threshold value. To achieve a detectable surface-morphology change, i.e., a larger buckling displacement, it is highly desirable to develop 2D piezoelectric materials with large piezoelectric coefficients d_{31} and d_{32}. Unfortunately, the available intrinsic 2D piezoelectric materials, such as GaP, InP, and $GaInSe_2$, have limited d_{31} and d_{32} in the range of 0.1–0.5 pm/V [31,32].

*junkai.deng@mail.xjtu.edu.cn
†zhe.liu@unimelb.edu.au

It has been proposed to introduce piezoelectric effects into intrinsically nonpiezoelectric graphene through atomic adsorption. Graphene has a 2D hexagonal structure with inversion symmetry and thus is not intrinsically piezoelectric. This inversion symmetry can be broken by the adsorption of atoms on the surface of graphene on only one side. This leads to piezoelectricity with piezoelectric coefficients d_{31} and d_{32}. Ong and Reed investigated the piezoelectricity of graphene doped with selected adatoms and obtained magnitudes of the piezoelectric coefficient d_{31} of around 0.3 pm/V [26]. Noor-A-Alam *et al.* found that codecoration of silicene with H and F generated a maximum d_{31} as high as 1.66 pm/V [33].

In this paper, we employ first-principles density-functional-theory (DFT) calculations to investigate the crystal structure, formation energy, and piezoelectric properties of black phosphorene (black P) with adatoms consisting of all metallic elements in the top three rows of the Periodic Table on its top surface, with a broad range of concentrations from $P_{48}X_1$ to P_4X_2. The adsorption-induced piezoelectric coefficient d_{31} varies from 0.12 to 6.28 pm/V. Notably, Li-doped black P has the largest d_{31} (6.28 pm/V), at least 4 times larger than that of any other 2D material. An in-depth analysis suggests that this considerable d_{31} value can be attributed to the low elastic modulus C_{11}. Using this material, we examine a prototypical design of surface-morphology engineering using finite-element-method (FEM) simulations. This demonstrates the promise of 2D piezoelectric materials in smart-surface applications.

II. METHODS

Our first-principles calculations are performed based on DFT, as implemented in the Vienna *ab initio* simulation package (VASP). Projector-augmented-wave pseudopotentials and the Perdew-Burke-Ernzerhof (PBE) exchange-correlation functional are adopted. For all calculations, the plane-wave cutoff is set at 800 eV. A Monkhorst-Pack gamma-centered k-point grid of dimensions $25 \times 15 \times 1$ is adopted for the black-P unit cell. The 2D black-P film is placed in the x-y plane. The supercell size in the z direction is fixed at 20 Å to avoid interactions between the black-P layers and their periodic images. In all cases, the atoms are fully relaxed in all directions until the force on each atom is less than 0.001 eV/Å, ensuring accuracy of the calculated piezoelectric strain. At 0.001 eV/Å, we observe a good linear relationship between the piezoelectric strain and the electric field strength applied. But at 0.01 eV/Å, a nonlinear relationship is obtained. A van der Waals (vdW) correction using the Tkatchenko-Scheffler method with iterative Hirshfeld partitioning is also applied to make a comparison.

III. RESULTS AND DISCUSSION

We first investigate a low-concentration adatom-phosphorene system with one adatom in a 4×3 orthorhombic phosphorene supercell (containing 48 P atoms), which we refer to as $P_{48}X_1$. Four types of metallic atom from the first three rows of the Periodic Table, i.e., alkali metals, alkaline-earth metals, transition metals, and other metals, which are listed at the top of Fig. 1, are selected. In the inset of Fig. 1, the most stable adsorption site is the hollow site (H site), where the adatom shifts away from the center of the hexagonal cell and forms three bonds with nearby P atoms. The results are consistent with previous results [34]. To examine the stability of the relaxed structure, we calculate the formation energy per adatom E_f, which is presented in the form of bar plots in Fig. 1. The formation energy per adatom is defined as $E_f = E_a - E_c$. Here, E_a is the adsorption energy, defined as $E_a = [E_{P_nX_m} - E_{P_n} - mE_X]/m$, where $E_{P_nX_m}$ is the total energy of the adatom-doped black-P supercell, with n phosphorene atoms and m metallic adatoms, E_{P_n} is the total energy of the pristine black P, and E_X is the energy of the isolated metal atom. E_c is the bulk cohesive energy of metal X, for which we use the experimental values given in Ref. [35]. Our calculated results are close to those of previous work [34], in which some metal adatoms from the first three rows of the Periodic Table (Li, Na, Mg, Al,

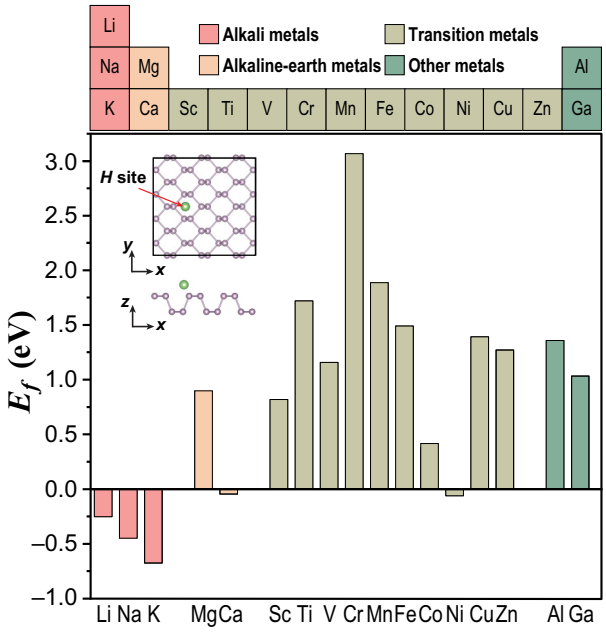

FIG. 1. Formation energy per adatom E_f of $P_{48}X_1$ calculated using DFT with the PBE functional. All metallic adatoms in the first three rows of the Periodic Table are examined, as shown at the top of the figure. All alkali adatoms have a negative E_f. For transition metals, only Ni, in the middle of the Periodic Table, have a negative E_f. The inset shows the most stable adsorption site, the hollow site.

Cr, Fe, Co, and Ni) were studied. Most of the alkali and alkaline-earth metals have a negative E_f value, with only one exception, Mg. For transition metals, only Ni shows a negative E_f value. A negative E_f value indicates that the adatom-doped black P is thermodynamically stable against phase separation into a black-P monolayer and metallic clusters.

Adatom-phosphorene systems with higher concentrations of adatoms, namely one or two adatoms per phosphorene unit cell (referred to as P_4X_1 and P_4X_2, respectively), are also investigated. For P_4X_1, the most stable adsorption site is the H site. All of the transition-metal adatoms (except Cu and Zn) are located at the center of the hollow site and form four bonds with neighboring P atoms. Other cases resemble the $P_{48}X_1$ system, where the adatom shifts away from the center. For P_4X_2, the adsorption geometry is more complicated. There are two hollow sites on one side of the black-P unit cell: the (0.0, 0.0) and (0.5, 0.5) sites in the x-y plane, as illustrated in Fig. 2. In most cases, the two adatoms are located at these two sites. The alkali and alkaline-earth metal adatoms form two layers, as shown in Fig. 2(b). But some transition-metal adatoms (Fe, Co, and Ni) form a single layer on top of the phosphorene. This kind of adsorption causes the ratio of the lattice constants b and a to become close to one. For example, pristine phosphorene has $b/a = 1.40$, whereas phosphorene doped with Fe, Co, and Ni has $b/a = 1.05$, 1.04, and 1.05, respectively. For atoms on the right of the Periodic Table (Zn, Al, and Ga), Fig. 2(c) shows that the most stable site is on top of a P atom (T site).

Figure 2(a) shows the results for E_f of P_4X_1 and P_4X_2. Most of the alkali and alkaline-earth metals have a negative

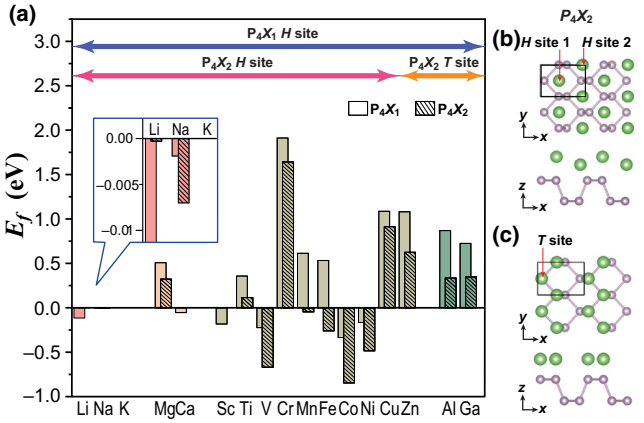

FIG. 2. (a) Formation energy per adatom E_f of P_4X_1 and P_4X_2. All metallic adatoms in the first three rows of the Periodic Table are tested. The inset shows an enlarged view for the cases of Li and Na. (b) Crystal structure of P_4X_2 with adatoms on two hollow sites. (c) Crystal structure of P_4X_2 with adatoms on two top sites. Most alkali metals have a negative E_f. With an increase in concentration, E_f for transition-metal adatoms, Al, and Ga tends to shift to more negative values.

E_f for both compositions. But for K and Ca, the crystal structure of P_4X_2 exhibits drastic changes, and the black-P lattice backbone is completely broken. For the transition metals and for Al and Ga, E_f shows a trend toward a more negative value with an increase in concentration. In some cases, E_f changes from a positive to a negative value, which is not often seen in alloy systems. As such, we have 14 cases with a negative E_f for P_4X_1 and P_4X_2, whereas there are only five cases with a negative E_f for $P_{48}X_1$.

To examine the influence of vdW interactions on the calculated E_f values, we adopt the popular DFT–Tkatchenko-Scheffler (DFT-TS) scheme for the seven P_4X_2 systems with a negative E_f. As expected, their E_f values become more negative, with a nearly constant change of -0.5 to -0.6 eV/adatom compared with the results obtained from the PBE functional. This trend is consistent with our previous study of gas adsorption in some zeolites [36]. DFT-TS calculations might identify more cases with a negative formation energy. However, it should be noted that vdW-DFT calculations tend to overcorrect for the contribution from vdW interactions [36]. Thus, in the following, we focus on the 14 thermodynamically stable cases identified from our PBE calculations.

Adatom adsorption on one side breaks the inversion symmetry of black P, generating an out-of-plane electric polarization and consequent piezoelectricity. We calculate the piezoelectric coefficients of those 14 P_4X_1 and P_4X_2 cases. Figure 3 shows the in-plane piezoelectric strains ε_{11} and ε_{22} as functions of an applied electric field in the z direction. The electric field varies from -0.1 to 0.1 eV/Å for the seven P_4X_2 systems; this range of values can be achieved in experiments [37]. Figures 3(a) and 3(b) depict a good linear relationship between the strain and the electric field strength. The strain piezoelectric coefficients d_{31} and d_{32} can then be determined from the slope. The calculated values of d_{31} and d_{32} for P_4X_1 and P_4X_2 are listed in Fig. 4 and Table I. The results for P_4X_2 obtained from the DFT-TS calculations are also included in Table I.

Figure 4 compares the piezoelectric coefficients d_{31} of our materials with all previously reported values for 2D piezoelectric materials. Note that P_4Li_2 has a coefficient d_{31} much higher than that of other 2D materials, such as adatom-doped graphene (0.002–0.3 pm/V) [26], graphene oxide (0.24 pm/V) [27], InP (0.39 pm/V) [31], and H- and F-codecorated silicene (0.22–1.66 pm/V) [33]. The filled and unfilled bars represent adatom-induced piezoelectric materials and intrinsic piezoelectric materials, respectively. We find that the extrinsic adatom-induced materials often have larger d_{31} values than the intrinsic piezoelectric materials. A high adatom concentration usually leads to a higher d_{31}, except for V and Co. Such a coverage-concentration dependence is consistent with results for the adatom-doped graphene system [26]. The piezoelectric anisotropy is also significant for both P_4X_2

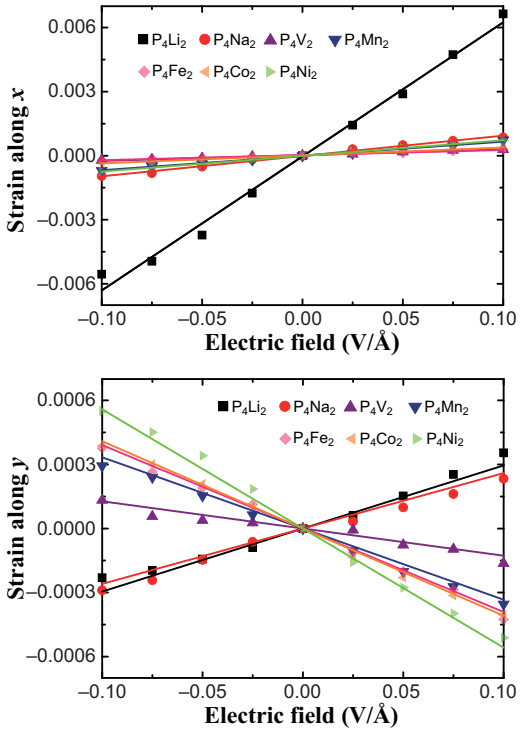

FIG. 3. In-plane piezoelectric strains in the x and y directions under an electric field applied perpendicular to the black-P plane (along the z direction) for P_4X_2.

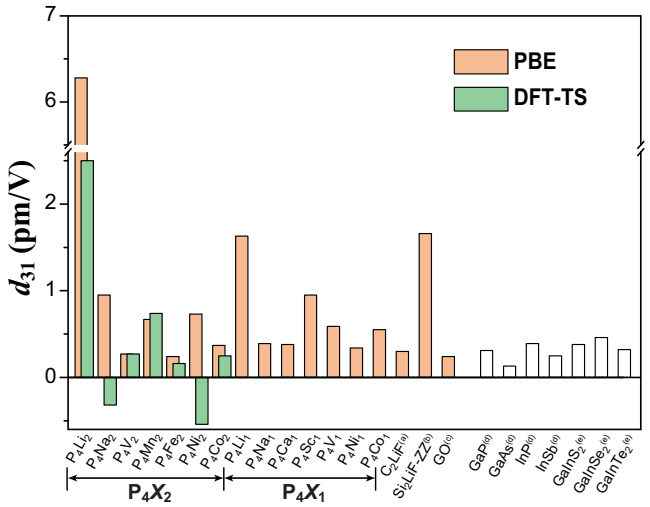

FIG. 4. Comparison of piezoelectric coefficients d_{31} of our adatom-doped black P with previously known values for 2D piezoelectric materials. The orange and green bars represent values of d_{31} calculated using the PBE functional and the DFT-TS scheme, respectively. GO denotes the graphene oxide. The color-filled and unfilled bars represent adatom-induced piezoelectric materials and intrinsic piezoelectric materials, respectively. The superscript labels "(a)," "(b)," "(c)," "(d)," and "(e)" refer to Refs. [26], [33], [27], [31], and [32], respectively.

and P_4X_1. P_4Li_2 has the largest d_{31}/d_{32} ratio, with a value of 21.

Compared with the PBE results, our DFT-TS calculations show that the d_{31} values of P_4V_2 and P_4Mn_2 increase, while for the other P_4X_2 materials, d_{31} is reduced. Besides, the d_{31} values of P_4Na_2 and P_4Ni_2 change from a positive to a negative value. There is no clear trend in the change in d_{31} obtained using different DFT computational methods. Although the d_{31} value of P_4Li_2 is reduced from 6.28 to 2.5 pm/V, it is still the highest among all reported materials. It is worth noting that the piezoelectric coefficients of the other 2D materials were calculated without a vdW correction [26,27,31–33].

TABLE I. Piezoelectric coefficients of P_4X_2 calculated using DFT. Units: pm/V. The PBE functional is adopted. To correct for the van der Waals interaction, we also perform DFT-TS calculations.

	d_{31} (PBE)	d_{32} (PBE)	d_{31} (DFT-TS)	d_{32} (DFT-TS)
P_4Li_2	6.28	0.30	2.50	−0.42
P_4Na_2	0.95	−0.26	−0.32	0.07
P_4V_2	0.27	0.13	0.27	0.36
P_4Mn_2	0.67	0.33	0.74	0.42
P_4Fe_2	0.24	0.39	0.16	0.36
P_4Ni_2	0.73	0.56	0.54	0.40
P_4Co_2	0.37	0.41	0.25	0.36

After a careful study of the results shown in Fig. 4 and Tables I, we do not find clear clues about how d_{31} depends on the adatom type. To obtain some understanding of the high d_{31} value of P_4Li_2, we perform the following analysis. The piezoelectric coefficients e_{31} and e_{32} describe the change in electric polarization as a result of applied in-plane mechanical strains. They are the key physical properties for mechanical-sensing applications. The most reliable way to calculate the electric polarization is to use the Berry-phase method. However, this requires a highly symmetric nonpolarized phase as a reference, which is not available in our study. Therefore, we adopt another way to calculate these coefficients. For 2D materials, there is a relation between the piezoelectric coefficients d_{ij} and e_{ij},

$$\begin{aligned} e_{31} &= d_{31}C_{11} + d_{32}C_{21}, \\ e_{32} &= d_{31}C_{12} + d_{32}C_{22}, \end{aligned} \tag{1}$$

where C_{11}, C_{22}, and C_{12} $(= C_{21})$ are the elastic stiffness constants. We determine the elastic constants of P_4X_2 by fitting the strain energy density $U(\varepsilon_{11}, \varepsilon_{22})$ calculated using the DFT method via

$$U(\varepsilon_{11}, \varepsilon_{22}) = \frac{1}{2}C_{11}\varepsilon_{11}^2 + \frac{1}{2}C_{22}\varepsilon_{22}^2 + C_{12}\varepsilon_{11}\varepsilon_{22}. \tag{2}$$

TABLE II. Piezoelectric coefficients, elastic stiffness constants, Young's modulus, and Poisson's ratio for P_4X_2 calculated using DFT computational method with PBE functional.

	P_4Li_2	P_4Na_2	P_4V_2	P_4Mn_2	P_4Fe_2	P_4Ni_2	P_4Co_2
e_{31} (10^{-10} C/m)	0.84	0.12	0.25	0.59	0.48	0.62	0.45
e_{32} (10^{-10} C/m)	0.90	−0.09	0.27	0.56	0.71	0.59	0.58
C_{11} (N/m)	13.01	18.11	78.80	72.58	115.76	76.99	98.61
C_{22} (N/m)	110.28	112.61	144.61	103.53	150.52	91.26	123.59
C_{12} (N/m)	9.03	21.68	30.50	32.66	52.89	10.44	20.93
E_x (N/m)	11.85	14.06	72.29	62.47	95.78	77.11	92.74
E_y (N/m)	107.52	85.87	132.80	88.84	128.11	88.29	122.06
υ_{xy}	0.08	0.19	0.21	0.32	0.35	0.11	0.17
υ_{yx}	0.69	1.20	0.39	0.45	0.35	0.14	0.21

Young's modulus E and Poisson's ratio ν are then calculated using

$$E_x = \frac{C_{11}C_{22} - C_{12}C_{21}}{C_{22}}, E_y = \frac{C_{11}C_{22} - C_{12}C_{21}}{C_{11}},$$
$$\nu_{xy} = \frac{C_{21}}{C_{22}}, \quad \nu_{yx} = \frac{C_{12}}{C_{11}}. \tag{3}$$

By substituting the calculated elastic constants into Eq. (1), the piezoelectric coefficients e_{31} and e_{32} can be determined. The results are summarized in Table II. Combining Eqs. (1) and (3) yields

$$d_{31} = \frac{e_{31}C_{22} - e_{32}C_{21}}{C_{11}C_{22} - C_{12}^2} = \frac{e_{31} - \nu_{xy}e_{32}}{C_{11} - \nu_{xy}C_{12}}, \tag{4}$$

$$d_{32} = \frac{e_{31}C_{12} - e_{32}C_{11}}{C_{12}^2 - C_{11}C_{22}} = \frac{-C_{11}(e_{31}\nu_{yx} - e_{32})}{C_{11}C_{22} - C_{12}^2}. \tag{5}$$

In Table II, we note that these P_4X_2 materials have $C_{11} \gg \nu_{xy}C_{12}$ and $e_{31} \gg \nu_{xy}e_{32}$. Hence Eq. (4) can be simplified to $d_{31} \approx e_{31}/C_{11}$. P_4Li_2 has the highest e_{31} but the smallest C_{11} among all the cases. It thus has the highest d_{31} value. The low stiffness C_{11} of P_4Li_2 might be related to its significantly increased lattice constant a compared with pristine black P, 4.88 Å vs 4.62 Å. The Li adatoms could significantly distort the chemical bonds in black P, leading to a reduced stiffness C_{11}.

Finally, we carry out FEM simulations to demonstrate a prototypical smart-surface design using the 2D piezoelectric material P_4Li_2. Figure 5(a) illustrates the prototype, where a square film of monolayer P_4Li_2 with an edge size L is placed on a substrate. The four edges are fixed to the substrate. A local voltage is applied in the vertical direction to a selected square region of the thin film with an edge size l. The large piezoelectric coefficient d_{31} of P_4Li_2 should lead to a large in-plane strain ε_{11} in the selected region and a subsequent large out-of-plane buckling displacement. This could generate a detectable morphology change on the surface.

In our FEM model [Fig. 5(b)], four-point shell elements with a mesh size of about 0.008–0.01 mm and a thickness of 4.6×10^{-4} μm are employed to simulate a thin film with the elastic properties of P_4Li_2 listed in Table II. The substrate is assumed to be rigid. The film-substrate interface is modeled assuming a cohesion mode with normal stiffness $K_n = 120$ MPa/mm, shear stiffness $K_t = 120$ MPa/mm, maximum normal separation stress $\delta n = 0.008$ MPa, maximum shear separation stress $\delta t = 0.01$ MPa, and adhesive energy $e = 8 \times 10^{-5}$ mJ. These effective parameters depend on the properties of the cohesive surfaces and the substrate [38,39]. They are selected to mimic the case of separating a bilayer of black P. A film-substrate separation could take place when the interfacial normal stress or energy-release rate is above a critical value. In our FEM simulations, the in-plane piezoelectric strain is simulated by a thermal-expansion strain with an appropriate expansion coefficient and temperature field applied in the P_4Li_2 film. We perform the FEM simulations using Abaqus/Explicit. A periodic boundary condition is applied to the four edges. The left plot in Fig. 5(b) shows the initial undeformed geometry. The right plot shows the swollen surface morphology obtained as a result of the out-of-plane elastic buckling displacement (for $L = 1$ mm and $l = 0.4$ mm). The arched swelling profile generated shows differences between the x and y directions. This can be attributed to the intrinsic elastic and piezoelectric anisotropy of P_4Li_2. The maximum swelling height is denoted by H.

To evaluate the dependence of H on the parameters L and l, a series of FEM calculations are carried out. Figure 5(c) summarizes the calculated results for H, with L varying from 0.5 to 5 mm and the ratio l/L varying from 0.1 to 0.8. Note that the in-plane piezoelectric strains are $\varepsilon_{11} = 0.628\%$ and $\varepsilon_{22} = 0.03\%$ in all cases. The swelling height H can reach up to 0.22 mm for $L = 5$ mm and $a/L = 0.8$. Previous studies have shown that receptors in the human finger can feel a texture by detecting surface roughness with a spatial resolution of about 40 μm over a contact area of 1 cm^2 [40]. Tactile features have been introduced in many banknotes to assist visually disabled people,

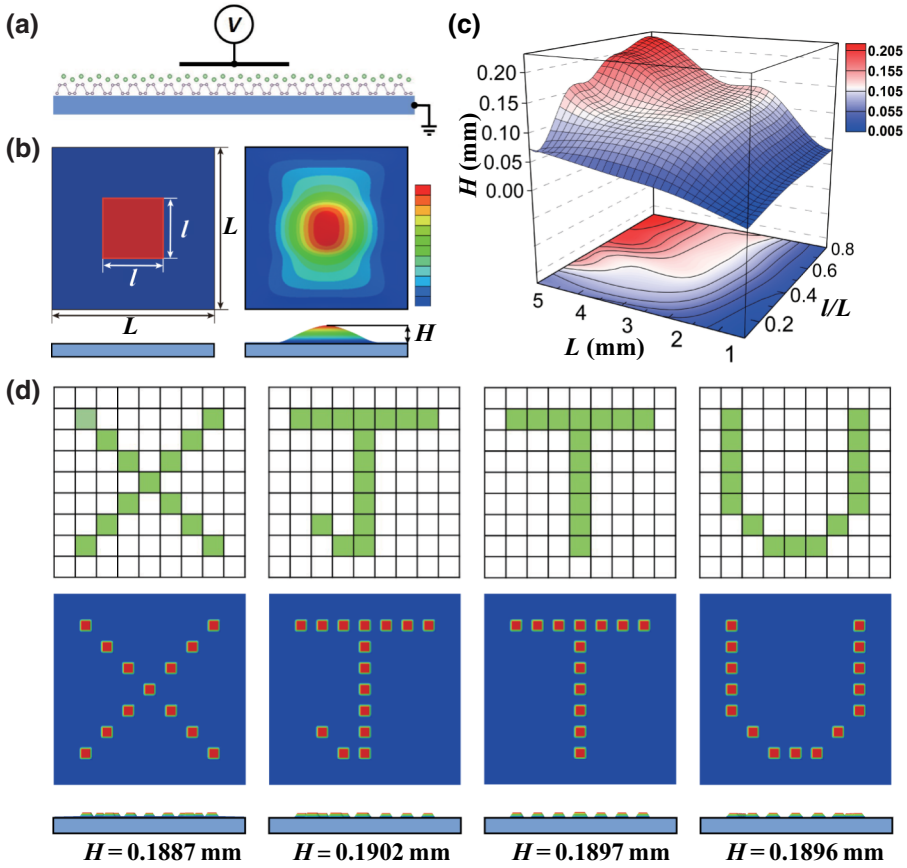

FIG. 5. Prototypical smart-surface design where P_4Li_2 is used to generate morphology changes under an external electric field, simulated via FEM. (a) Illustration of the design. A 2D P_4Li_2 monolayer thin film is placed on a rigid substrate with a vertical electric field applied locally. (b) Top view of our FEM model. The P_4Li_2 thin film has an edge length of L. The four edges are fixed to the substrate. The vertical electric field is applied to a local region in the center with edge size l. See the main text for details of our FEM model. The right part of (b) shows the surface swelling profile. (c) Maximum swelling height H as a function of L and l/L. The piezoelectric strains are $\varepsilon_{11} = 0.628\%$ and $\varepsilon_{22} = 0.03\%$. (d) Four arrays of 9×9 building blocks (pixels) assembled together. Each building block follows the prototypical design shown in (b). When a voltage is applied to selected blocks, the swollen blocks form patterns with special morphologies. In this case, the patterns are "X," "J," "T," "U."

for whom the depth that can be felt is about 50 μm [41]. These requirements can be feasibly achieved by selecting appropriate L and l/L values using Fig. 5(c).

Taking the prototype of the square thin film in Fig. 5(b) as one building block (or pixel), we can combine many such building blocks together to form an array, e.g., a 9×9 array as shown in Fig. 5(d). As a demonstration, here L and l/L are set to 5 mm and 0.5, respectively. Applying a vertical electric field to selected pixels leads to a designed morphology pattern on the surface. Figure 5(d) shows an example of patterns "X," "J," "T," "U," representing the initials of Xi'an Jiaotong University. Piezoelectric strains are applied only to the green blocks shown in the top plot in Fig. 5(d). The swelling patterns "X," "J," "T," "U" in our FEM simulations are observed in the bottom part (which shows a top view). In a side view, the height H generated is about 0.19 mm, which is large enough for many applications (e.g., detection by fingers). Recently, layer-by-layer assembly of multilayer 2D materials, e.g., vdW heterostructures, has been widely demonstrated in many publications [19]. This can be used to fabricate a heterostructure composed of a P_4X_2 layer on top of a graphene electrode layer. The lithographic technology for patterning graphene layers and layers of other conductive 2D materials is also mature [42]. This technology can be used to fabricate top electrode layers with required patterns, e.g., a 9×9 pixel array. Using available transfer techniques [43], a patterned top electrode layer could be placed on top of P_4X_2. All of these experimental technologies are readily available, suggesting the feasibility of our prototypical design based on piezoelectric P_4X_2 (or other 2D piezoelectric materials) in experiments. Using 2D piezoelectric materials to design surface-morphology changes is promising for smart-surface applications.

IV. CONCLUSIONS

In summary, using DFT-PBE calculations, we investigate the crystal structure, formation energy, and piezoelectric properties of adatoms doped on the top surface of black phosphorene. Adatoms X consisting of all metallic elements in the top three rows of the Periodic Table, and concentrations ranging from $P_{48}X_1$ to P_4X_2 are considered. In most cases, the metal adatoms occupy the H sites. But at high concentrations, in P_4X_2, Zn, Al, and Ga adatoms occupy the T sites. For $P_{48}X_1$, P_4X_1, and P_4X_2, there are five, seven, and seven types, respectively, of adatoms with a negative formation energy. We find that the piezoelectric coefficient d_{31} of P_4Li_2 is at least 4 times higher than those of all other 2D materials. Detailed analysis attributes the superior piezoelectric properties of this material to its small elastic constant C_{11}. The excellent piezoelectricity of

adatom-doped black P could be used to generate significant in-plane strain under an applied electric field in the vertical direction. The elastic-buckling-induced out-of-plane swelling patterns can be used in smart-surface applications. We use FEM simulations to successfully demonstrate a prototypical smart-surface design. The design of surface morphologies using 2D piezoelectric materials is a promising avenue for smart surfaces.

ACKNOWLEDGMENTS

The authors gratefully acknowledge support from the NSFC (Grants No. 11974269 and No. 51728203) and support from the 111 Project 2.0 (Grant No. BP2018008). J.D. also thanks the National Key R&D Program of China (Grant No. 2018YFB1900104), and the Fundamental Research Funds for the Central Universities for support. J.Z.L. acknowledges support from the ARC Discovery Projects (Grant No. DP180101744), and high-performance computing (HPC) from the National Computational Infrastructure of Australia. This work is also supported by the State Key Laboratory for Mechanical Behavior of Materials. The authors would also like to thank Dr. X.D. Zhang and Mr. F. Yang at the Network Information Center of Xi'an Jiaotong University for support of the HPC platform.

[1] F. Zhou and W. T. S. Huck, Surface grafted polymer brushes as ideal building blocks for "smart" surfaces, Phys. Chem. Chem. Phys. **8**, 3815 (2006).

[2] G. Ju, M. Cheng, and F. Shi, A pH-responsive smart surface for the continuous separation of oil/water/oil ternary mixtures, NPG Asia Mater. **6**, e111 (2014).

[3] N. S. Pesika, H. Zeng, K. Kristiansen, B. Zhao, Y. Tian, K. Autumn, and J. Israelachvili, Gecko adhesion pad: A smart surface? J. Phys.: Condens. Matter **21**, 464132 (2009).

[4] Y. Wang, A. Villada, Y. Zhai, Z. N. Zou, Y. Z. Chen, X. B. Yin, and J. L. Xiao, Tunable surface wrinkling on shape memory polymers with application in smart micromirror, Appl. Phys. Lett. **114**, 193701 (2019).

[5] H. Merlitz, G. L. He, C. X. Wu, and J. U. Sommer, Nanoscale Brushes: How to Build a Smart Surface Coating, Phys. Rev. Lett. **102**, 115702 (2009).

[6] E. Mele, D. Pisignano, M. Varda, M. Farsari, G. Filippidis, C. Fotakis, A. Athanassiou, and R. Cingolani, Smart photochromic gratings with switchable wettability realized by green-light interferometry, Appl. Phys. Lett. **88**, 203124 (2006).

[7] D. Shin, Y. Urzhumov, Y. Jung, G. Kang, S. Baek, M. Choi, H. Park, K. Kim, and D. R. Smith, Broadband electromagnetic cloaking with smart metamaterials, Nat. Commun. **3**, 1213 (2012).

[8] H. Assender, V. Bliznyuk, and K. Porfyrakis, How surface topography relates to materials' properties, Science **297**, 973 (2002).

[9] S. Z. Wu, J. N. Wang, L. G. Niu, J. Yao, D. Wu, and A. W. Li, Reversible switching between isotropic and anisotropic wetting by one-direction curvature tuning on flexible superhydrophobic surfaces, Appl. Phys. Lett. **98**, 081902 (2011).

[10] E. P. Chan, E. J. Smith, R. C. Hayward, and A. J. Crosby, Surface wrinkles for smart adhesion, Adv. Mater. **20**, 711 (2008).

[11] D. Terwagne, M. Brojan, and P. M. Reis, Smart morphable surfaces for aerodynamic drag control, Adv. Mater. **26**, 6608 (2014).

[12] D. L. Huber, R. P. Manginell, M. A. Samara, B.-I. Kim, and B. C. Bunker, Programmed adsorption and release of proteins in a microfluidic device, Science **301**, 352 (2003).

[13] U. Kim, J. Kang, C. Lee, H. Y. Kwon, S. Hwang, H. Moon, J. C. Koo, J.-D. Nam, B. H. Hong, J.-B. Choi, and H. R. Choi, A transparent and stretchable graphene-based actuator for tactile display, Nanotechnology **24**, 145501 (2013).

[14] C. L. Holloway, M. A. Mohamed, E. F. Kuester, and A. Dienstfrey, Reflection and transmission properties of a metafilm: With an application to a controllable surface composed of resonant particles, IEEE Trans. Electromagn. Compat. **47**, 853 (2005).

[15] J. Deng, Z. Chang, T. Zhao, X. Ding, J. Sun, and J. Z. Liu, Electric field induced reversible phase transition in Li doped phosphorene: Shape memory effect and superelasticity, J. Am. Chem. Soc. **138**, 4772 (2016).

[16] C. Cui, F. Xue, W.-J. Hu, and L.-J. Li, Two-dimensional materials with piezoelectric and ferroelectric functionalities, NPJ 2D Mater. Appl. **2**, 18 (2018).

[17] G. W. Rogers and J. Z. Liu, Graphene actuators: Quantum-mechanical and electrostatic double-layer effects, J. Am. Chem. Soc. **133**, 10858 (2011).

[18] Z. Chang, J. Deng, G. G. Chandrakumara, W. Yan, and J. Z. Liu, Two-dimensional shape memory graphene oxide, Nat. Commun. **7**, 11972 (2016).

[19] K. S. Novoselov, A. Mishchenko, A. Carvalho, and A. H. Castro Neto, 2D materials and van der Waals heterostructures, Science **353**, aac9439 (2016).

[20] P. Rivera, K. L. Seyler, H. Yu, J. R. Schaibley, J. Yan, D. G. Mandrus, W. Yao, and X. Xu, Valley-polarized exciton dynamics in a 2D semiconductor heterostructure, Science **351**, 688 (2016).

[21] B. Cho, J. Yoon, S. K. Lim, A. R. Kim, D. H. Kim, S. G. Park, J. D. Kwon, Y. J. Lee, K. H. Lee, B. H. Lee, H. C. Ko, and M. G. Hahm, Chemical sensing of 2D graphene/MoS_2 heterostructure device, ACS Appl. Mater. Interfaces **7**, 16775 (2015).

[22] L. Song, L. Ci, H. Lu, P. B. Sorokin, C. Jin, J. Ni, A. G. Kvashnin, D. G. Kvashnin, J. Lou, B. I. Yakobson, and P. M. Ajayan, Large scale growth and characterization of atomic hexagonal boron nitride layers, Nano Lett. **10**, 3209 (2010).

[23] A. Castellanos-Gomez, M. Poot, G. A. Steele, H. S. J. van der Zant, N. Agrait, and G. Rubio-Bollinger, Elastic properties of freely suspended MoS_2 nanosheets, Adv. Mater. **24**, 772 (2012).

[24] C. Lee, X. Wei, J. W. Kysar, and J. Hone, Measurement of the elastic properties and intrinsic strength of monolayer graphene, Science **321**, 385 (2008).

[25] Q. Wei and X. H. Peng, Superior mechanical flexibility of phosphorene and few-layer black phosphorus, Appl. Phys. Lett. **104**, 251915 (2014).

[26] M. T. Ong and E. J. Reed, Engineered piezoelectricity in graphene, ACS Nano **6**, 1387 (2012).
[27] Z. Y. Chang, W. Y. Yan, J. Shang, and J. Z. Liu, Piezoelectric properties of graphene oxide: A first-principles computational study, Appl. Phys. Lett. **105**, 023103 (2014).
[28] K.-A. N. Duerloo, M. T. Ong, and E. J. Reed, Intrinsic piezoelectricity in two-dimensional materials, J. Phys. Chem. Lett. **3**, 2871 (2012).
[29] W. Wu, L. Wang, Y. Li, F. Zhang, L. Lin, S. Niu, D. Chenet, X. Zhang, Y. Hao, T. F. Heinz, J. Hone, and Z. L. Wang, Piezoelectricity of single-atomic-layer MoS_2 for energy conversion and piezotronics, Nature **514**, 470 (2014).
[30] R. Fei, W. Li, J. Li, and L. Yang, Giant piezoelectricity of monolayer group IV monochalcogenides: SnSe, SnS, GeSe, and GeS, Appl. Phys. Lett. **107**, 173104 (2015).
[31] M. N. Blonsky, H. L. Zhuang, A. K. Singh, and R. G. Hennig, Ab initio prediction of piezoelectricity in two-dimensional materials, ACS Nano **9**, 9885 (2015).
[32] Y. Guo, S. Zhou, Y. Bai, and J. Zhao, Enhanced piezoelectric effect in janus group-III chalcogenide monolayers, Appl. Phys. Lett. **110**, 163102 (2017).
[33] M. Noor-A-Alam, H. J. Kim, and Y.-H. Shin, Hydrogen and fluorine co-decorated silicene: A first principles study of piezoelectric properties, J. Appl. Phys. **117**, 224304 (2015).
[34] T. Hu and J. Hong, First-principles study of metal adatom adsorption on black phosphorene, J. Phys. Chem. C **119**, 8199 (2015).
[35] C. Kittel *et al.*, *Introduction to Solid State Physics* (Wiley, Hoboken, NJ, 2005), 8th ed., Vol. 8.
[36] J. Shang, G. Li, R. Singh, P. Xiao, D. Danaci, J. Z. Liu, and P. A. Webley, Adsorption of CO_2, N_2, and CH_2 in Cs-exchanged chabazite: A combination of van der Waals density functional theory calculations and experiment study, J. Chem. Phys. **140**, 084705 (2014).
[37] Y. Zhang, T. T. Tang, C. Girit, Z. Hao, M. C. Martin, A. Zettl, M. F. Crommie, Y. R. Shen, and F. Wang, Direct observation of a widely tunable bandgap in bilayer graphene, Nature **459**, 820 (2009).
[38] W. Tan, F. Naya, L. Yang, T. Chang, B. Falzon, L. Zhan, J. Molina-Aldareguía, C. González, and J. Llorca, The role of interfacial properties on the intralaminar and interlaminar damage behaviour of unidirectional composite laminates: Experimental characterization and multiscale modelling, Compos. B: Eng. **138**, 206 (2018).
[39] A. Hussein and B. Kim, Micromechanics based FEM study on the mechanical properties and damage of epoxy reinforced with graphene based nanoplatelets, Compos. Struct. **215**, 266 (2019).
[40] J. Morley, A. Goodwin, and I. Darian-Smith, Tactile discrimination of gratings, Exp. Brain Res. **49**, 291 (1983).
[41] N. R. Council *et al.*, *Currency Features for Visually Impaired People* (National Academies Press, Washington, DC, 1995), Vol. 478.
[42] Y. Zhou and K. P. Loh, Making patterns on graphene, Adv. Mater. **22**, 3615 (2010).
[43] A. Castellanos-Gomez, M. Buscema, R. Molenaar, V. Singh, L. Janssen, H. S. Van Der Zant, and G. A. Steele, Deterministic transfer of two-dimensional materials by all-dry viscoelastic stamping, 2D Mater. **1**, 011002 (2014).